

Interpretable AI-Assisted Early Reliability Prediction for a Two-Parameter Parallel Root-Finding Scheme

Bruno Carpentieri^{*4}, Andrei Velichko³, Mudassir Shams^{1,2}, and Paola Lecca⁴

¹Department of Mathematics, Faculty of Arts and Science, Balıkesir University, 10145 Balıkesir, Turkey; mudassir.shams@balikesir.edu.tr

²Department of Mathematics and Statistics, Riphah International University, I-14, Islamabad 44000, Pakistan

³Institute of Physics and Technology, Petrozavodsk State University, 185910 Petrozavodsk, Russia; velichko@petsu.ru

⁴Faculty of Engineering, Free University of Bozen–Bolzano, 39100 Bolzano, Italy

Abstract

We propose an interpretable AI-assisted reliability diagnostic framework for parameterized root-finding schemes based on kNN–LLE proxy stability profiling and multi-horizon early prediction. The approach augments a numerical solver with a lightweight predictive layer that estimates solver reliability from short prefixes of iteration dynamics, enabling early identification of stable and unstable parameter regimes. For each configuration in the parameter space, raw and smoothed proxy profiles of a largest Lyapunov exponent (LLE) estimator are constructed, from which contractivity-based reliability scores summarizing finite-time convergence are derived. Machine learning models predict the reliability score from early segments of the proxy profile, allowing the framework to determine when solver dynamics become diagnostically informative. Experiments on a two-parameter parallel root-finding scheme show reliable prediction after only a few iterations: the best models achieve $R^2 \approx 0.48$ at horizon $T = 1$, improve to $R^2 \approx 0.67$ by $T = 3$, and exceed $R^2 \approx 0.89$ before the characteristic minimum-location scale of the stability profile. Prediction accuracy increases to $R^2 \approx 0.96$ at larger horizons, with mean absolute errors around 0.03, while inference costs remain negligible (microseconds per sample). The framework provides interpretable stability indicators and supports early decisions during solver execution, such as continuing, restarting, or adjusting parameters.

Keywords: interpretable artificial intelligence; scientific machine learning; solver reliability prediction; root-finding algorithms; biomedical modeling

1 Introduction

Robust and reliable root-finding remains a central building block in scientific computing, underpinning nonlinear optimization, inverse problems, parameter estimation, and the solution of discretized PDE models [1, 2, 3]. In many applications, the practical performance of an iterative solver depends not only on the underlying function f and the initialization, but also on algorithmic hyperparameters (e.g., damping, step control, restart policies) and on the sensitivity of the iteration

^{*}Correspondence: bruno.carpentieri@unibz.it

map to perturbations. This sensitivity is especially pronounced in high-order and parameterized iterative schemes, where the convergence dynamics may change significantly with the choice of internal parameters [4]. Consequently, there is growing interest in diagnostic layers that can (i) map stability and reliability across parameter domains, and (ii) provide early predictions of solver behavior to reduce wasted computation and enable adaptive control.

In many biomedical and physiological modelling tasks, nonlinear equation solvers are embedded within larger computational pipelines, for example in parameter estimation for pharmacokinetic models [5, 6], inverse problems in bioheat transfer, electrophysiological simulations, or models of neural dynamics [7, 8]. In these settings, the reliability of the numerical solver plays a critical role: unstable iterations or convergence to non-physical solutions may propagate through the modelling workflow and lead to misleading quantitative conclusions [9]. Moreover, biomedical models are often highly sensitive to parameter variations, making the behavior of the solver difficult to predict a priori. Biological models spanning from biochemical reaction networks to disease spread simulations, often exhibit complex behaviors where small input perturbations result in substantial changes to outputs. This sensitivity stems from the inherent complexity of biological systems, which are often modeled with large numbers of free parameters that significantly affect model behavior. There are three key reasons for the high sensitivity to parameters as follows. (i) The nonlinear dynamics: biological processes, such as metabolic pathways or gene regulation, often involve nonlinear relationships (e.g., sigmoid curves), meaning small changes in a parameter can lead to a shift from negligible to maximum impact. (ii) The large number of connections between network nodes meaning that small changes in one parameter can cascade through networks, amplifying over time and space, causing significant phenotypic or ecological shifts. (iii) The structural sensitivity meaning that biological models are often highly sensitive to the specific mathematical functions used to describe processes (like growth or mortality), not just the parameter values, which can lead to divergent predictions. These challenges motivate the development of diagnostic layers that provide transparent and interpretable indicators of solver reliability. By detecting instability early and guiding parameter selection, such tools can contribute to more trustworthy computational pipelines in biomedical modelling.

Machine learning (ML) has recently become a prominent tool for enhancing nonlinear solvers and numerical algorithms more broadly [10]. The literature largely clusters into four complementary directions. First, learned warm-starts use regression models (often neural networks) to provide high-quality initial guesses and improve basin selection, which can significantly reduce iterations and failure rates in simultaneous or high-order schemes [11, 12, 13, 14]. Second, surrogate-assisted solving replaces expensive solver components with learned approximations, for example through physics-informed neural networks (PINNs) or operator-learning frameworks [15, 16]. Third, solver control and adaptivity uses machine learning to tune discretization parameters or solver hyperparameters during runtime [17]. Fourth, early convergence or failure prediction analyzes short segments of iteration traces to forecast solver behavior and trigger restarts or parameter adjustments, often relying on indicators derived from the trajectory of the underlying iteration dynamics.

A closely related line of work explores trajectory-based stability indicators that characterize the dynamical behavior of iterative processes and can serve as informative signals for data-driven or machine-learning-based diagnostics. In particular, Lyapunov-exponent-based diagnostics and finite-time stability measures have long been used to characterize transient instability and chaotic behavior in nonlinear dynamical systems [18]. More recently, machine learning approaches have been proposed to estimate Lyapunov exponents directly from time-series data [19]. Related trajectory-driven diagnostics based on micro-ensemble perturbation analysis have also been studied for analyzing local stability and synchronization phenomena in nonlinear systems [20].

In the context of iterative numerical algorithms, these ideas naturally motivate trajectory-based

stability profiling approaches. Iterative solvers generate sequences of approximations whose evolution can be interpreted as a discrete dynamical system, making them particularly amenable to trajectory-based diagnostics. In particular, our recent study [21] introduced a finite-time contractivity profiling framework based on a kNN micro-series estimator of a largest Lyapunov exponent (LLE) proxy, enabling systematic exploration of parameter spaces in parallel root-finding schemes. That work demonstrated that profile-derived metrics such as S_{\min} and S_{mom} can be used to construct stability landscapes over (α, β) parameter grids and to identify regions associated with faster and more reliable convergence. Similar trajectory-driven diagnostics have also been explored for parameter optimization in parallel iterative methods through finite-time contraction profiling [22].

While these approaches provide systematic tools for parameter optimization and stability analysis, they do not address a complementary question that arises in practical computational workflows: whether the reliability of a solver configuration can be predicted early during the iteration process. In contrast to profiling-based approaches that require the full trajectory to assess solver stability, the present work investigates whether reliability can be predicted early from short prefixes of trajectory-derived stability indicators, thereby enabling lightweight AI-assisted diagnostics during solver execution. Importantly, the indicators used in this study retain a clear dynamical interpretation, providing interpretable signals linking solver behavior to stability properties of the underlying iteration process.

Despite these advances, several broader challenges remain in the integration of machine learning with numerical solvers. Generalization beyond the training distribution is often underexplored, interpretability may be limited, and empirical gains can sometimes be overstated when evaluated against weak baselines or under selective reporting [23]. These issues motivate approaches that retain a clear physical or dynamical interpretation and provide transparent diagnostics rather than black-box prescriptions.

The present paper addresses this gap by introducing an interpretable AI-augmented reliability diagnostic framework for a two-parameter parallel root-finding scheme. The method builds on kNN–LLE proxy profiles derived from early iteration dynamics and formulates a multi-horizon learning problem: can a profile-based reliability score S_{mom} be predicted accurately from only the first few raw proxy values? The answer is affirmative. Across both random and structured center-to-periphery splits over the (α, β) grid, we show that strong predictive performance is achieved from surprisingly short prefixes, with prediction quality improving rapidly as the horizon increases and saturating thereafter. Because the learning layer operates on interpretable stability indicators rather than raw trajectories, the resulting framework remains closely connected to the dynamical analysis of solver behavior.

The contributions of this work are fourfold:

1. We develop a unified computational pipeline that couples kNN–LLE proxy profiling, profile-derived reliability scoring, and multi-horizon supervised learning over a two-parameter solver domain.
2. We show that early prefixes of the raw proxy profile already contain substantial information about the final reliability score S_{mom} , enabling prediction before the characteristic minimum of the smoothed profile is observed.
3. We compare multiple standard regression models under both random and center-to-periphery splits, quantifying not only in-distribution accuracy but also extrapolative generalization across the parameter landscape.
4. We provide interpretable visual and statistical validation through profile examples, timing histograms, metric curves, and test-only heatmap reconstructions, thereby clarifying how the learned diagnostic layer relates to the underlying solver dynamics.

The remainder of the paper is organized as follows. Section 2 introduces the proposed framework,

including the underlying iterative scheme, the construction of the kNN–LLE proxy profiles, the profile-based reliability metrics, and the multi-horizon learning protocol. Section 3 presents the experimental design, including the parameter grid, profiling hyperparameters, and evaluation procedure. Section 4 reports the main empirical findings, combining profile-level illustrations, timing statistics, multi-horizon regression results, and heatmap-level validation under both random and center-to-periphery splits. Section 5 interprets these results from the viewpoints of early diagnosis, computational savings, interpretability, and generalization. Finally, Section 6 summarizes the main conclusions and outlines directions for future work.

2 Methodology

Figure 1 summarizes the overall computational pipeline used in this work. The workflow begins with profile generation on a two-parameter grid, where repeated solver runs are used to construct kNN–LLE proxy profiles and profile-derived reliability metrics. These profile traces are then converted into multi-horizon datasets by truncating the raw proxy profile at increasing prefix lengths T . Standard regression models are trained to predict the final reliability score S_{mom} from these early prefixes, enabling quantitative analysis of how soon solver reliability becomes predictable from early dynamics. The learned models are finally evaluated through metric curves and test-only heatmap reconstructions over the parameter domain.

2.1 Problem Setting and Iterative Scheme (Brief)

We consider nonlinear root-finding problems of the form

$$f(z) = 0, \tag{1}$$

where $f : \mathbb{R} \rightarrow \mathbb{R}$ (and, more generally, $f : \mathbb{R}^d \rightarrow \mathbb{R}^d$) may be nonlinear and parameter-dependent. The computational backbone is a derivative-free, parallel, two-parameter iterative scheme whose behavior depends on two control parameters (α, β) . For each fixed (α, β) , the solver generates an iterate sequence $\{z_k\}_{k \geq 0}$ from an initialization z_0 . The goal of the present study is to build an interpretable reliability layer around this solver rather than replacing the numerical scheme. Auxiliary solver-level validation under varied initial guesses, together with a comparison against existing parallel schemes, is reported in Appendix A. Those appendix experiments are carried out at a single representative parameter pair, $(\alpha, \beta) = (-0.1, 4.0)$, selected from the stable region of the (α, β) parameter map.

2.2 kNN–LLE Proxy Profile Construction

For each solver run we define a scalar micro-series that summarizes early iterative dynamics. In this study we use the log step norm

$$y_k = \log(\|z_{k+1} - z_k\|), \quad k = 0, 1, \dots, K - 1, \tag{2}$$

computed over a fixed horizon of K iterations. For a given (α, β) , an ensemble of independent runs yields a collection of micro-series.

To obtain a lightweight proxy for local stability, we estimate a kNN-based largest Lyapunov exponent (LLE) indicator from short windows of the micro-series. For each window end index t_{end} , delay-embedded vectors are built using a look-back length L and multiple prediction horizons

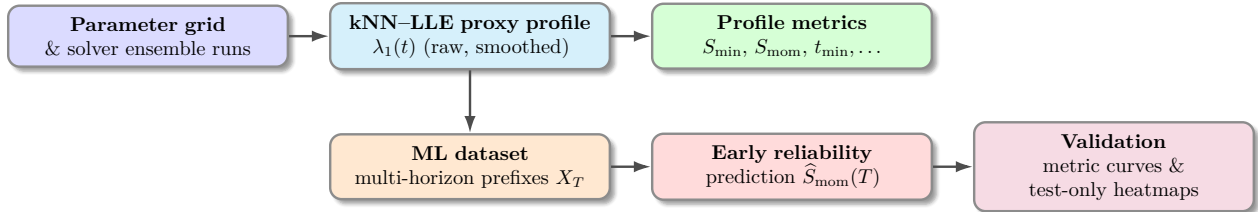


Figure 1: Conceptual pipeline of the proposed reliability diagnostic. Solver ensembles are generated on a (α, β) grid, yielding kNN-LLE proxy profiles and interpretable profile metrics. Multi-horizon prefixes form an ML dataset used for early prediction of $S_{\text{mom}}(T)$, followed by validation via metric curves and test-only heatmaps.

$h \in \{h_{\min}, \dots, h_{\max}\}$. The slope of the multi-horizon forecast error acts as a stability proxy, producing a profile

$$\lambda_1(t_{\text{end}}), \quad t_{\text{end}} = 1, 2, \dots, W, \quad (3)$$

where negative values indicate locally contractive dynamics and positive values indicate locally expansive behavior. A trailing-mean filter with window size W_{smooth} is applied to obtain a smoothed profile $\tilde{\lambda}_1(t)$.

2.3 Profile-Based Reliability Metrics

From $\tilde{\lambda}_1(t)$ we compute interpretable summary metrics capturing both depth and extent of contractive behavior. Let

$$t_{\min} = \arg \min_{t \in [t_{\text{start}}, t_{\text{end}}]} \tilde{\lambda}_1(t), \quad y_{\min} = \min_{t \in [t_{\text{start}}, t_{\text{end}}]} \tilde{\lambda}_1(t). \quad (4)$$

We define

$$S_{\min} = \frac{-y_{\min}}{t_{\min} + \varepsilon}, \quad (5)$$

and a negative-mass moment score

$$M_0 = \sum_t \max\{0, -\tilde{\lambda}_1(t)\}, \quad \bar{t} = \frac{\sum_t t \max\{0, -\tilde{\lambda}_1(t)\}}{M_0 + \varepsilon}, \quad S_{\text{mom}} = \frac{M_0}{\bar{t} + \varepsilon}, \quad (6)$$

where sums are taken over a fixed evaluation interval and $\varepsilon > 0$ is a small numerical constant. Intuitively, larger S_{mom} indicates earlier and stronger contractivity.

2.4 Dataset Construction for Multi-Horizon Learning

To predict S_{mom} without running the profiling procedure until the full minimum is observed, we define multi-horizon learning tasks using early prefixes of the raw profile. For each grid point (α, β) and each horizon T we define

$$X_T = [\lambda_1^{\text{raw}}(1), \lambda_1^{\text{raw}}(2), \dots, \lambda_1^{\text{raw}}(T)], \quad (7)$$

with target $y = S_{\text{mom}}$ computed from the smoothed profile. The set of horizons is $\mathcal{T} = \{1, 1 + \Delta_T, 1 + 2\Delta_T, \dots\}$ up to the available profile length.

2.5 Train/Test Splits: Random vs. Center-to-Periphery Generalization

We evaluate generalization using two complementary splitting strategies.

Random split. All grid points are shuffled and divided into training and test sets according to a fixed test fraction. This split assesses average-case generalization when training and test samples follow the same parameter distribution.

Center-to-periphery split. To probe extrapolation across parameter regimes, we compute each point’s normalized squared distance to the grid center in (α, β) and allocate the most central fraction to training, with peripheral points used for testing. This split stresses out-of-distribution behavior near regime boundaries.

2.6 Learning Models and Evaluation (Brief)

For each horizon T , we train a regressor to predict the reliability score S_{mom} from the early-prefix feature vector X_T . To cover complementary inductive biases and complexity levels, we consider five standard model families: (i) k-nearest neighbors (kNN) regression, which provides a local, instance-based predictor well suited to regime-dependent behaviors; (ii) Ridge regression (linear model with ℓ_2 regularization), which offers a stable baseline under correlated features; (iii) Elastic Net (combined ℓ_1/ℓ_2 regularization), which balances stability with sparse feature selection; (iv) Random Forest regression, an ensemble of decision trees capturing nonlinear interactions and heterogeneous regimes; and (v) Gradient Boosting regression, a sequential tree-ensemble that often achieves high accuracy by fitting additive corrections. For each T , models are trained independently to reflect the multi-horizon (early-exit) setting and to quantify how predictive quality evolves as more early profile information becomes available.

Model performance is reported using standard regression criteria on held-out test data. In the final manuscript we focus on three complementary metrics: MAE (mean absolute error) as a robust measure of typical absolute deviation, RMSE (root mean squared error) as a penalty for larger errors, and R^2 (coefficient of determination) as a scale-free indicator of explained variance. These metrics together characterize both absolute accuracy and overall predictive fidelity across the parameter grid.

3 Experimental Setup

3.1 Parameter Grid and Computational Budget

All experiments are performed over a two-parameter control grid (α, β) , with

$$\alpha \in [-3, 5], \quad \beta \in [-2, 4], \tag{8}$$

sampled on a uniform 60×60 grid. For each grid point, we generate an ensemble of $N_{\text{runs}} = 1000$ independent solver trajectories (distinct initializations) and run the iterative scheme for $K = 200$ iterations per trajectory. Unless stated otherwise, a fixed random seed is used to ensure exact reproducibility across runs.

3.2 Micro-Series Definition and Stabilization Settings

From each trajectory we construct the micro-series

$$y_k = \log(\|z_{k+1} - z_k\|), \quad k = 0, \dots, K - 1, \tag{9}$$

which is used as the input signal for kNN-LLE proxy estimation. To avoid numerical artifacts in extremely small step regimes, a log-domain tail floor is applied (freezing the tail after the floor is

reached). In addition, an adaptive stabilization mechanism is enabled only to prevent explosive divergence (e.g., hard bounds for divergence markers and a step cap when stabilization is active), while preserving the raw dynamics in non-explosive regimes.

3.3 kNN–LLE Proxy Hyperparameters

The kNN–LLE proxy profile $\lambda_1(t_{\text{end}})$ is computed using the following fixed hyperparameter configuration:

- look-back length (embedding depth): $L = 5$,
- forecast horizons: $h \in \{1, 2, 3, 4, 5\}$ (i.e., $h_{\min} = 1$, $h_{\max} = 5$, step 1),
- kNN neighborhood size: $k = 3$,
- internal train/test split for the micro-series predictor: 0.60/0.40.

The raw profile is smoothed by a trailing-mean filter with window size $W_{\text{smooth}} = 4$ to reduce small oscillations.

3.4 Metric Window and Reliability Targets

Profile-based metrics are evaluated on a fixed index window of the proxy profile. Specifically, we consider

$$t \in [t_{\text{start}}, t_{\text{end}}] = [10, 200], \quad (10)$$

where the effective start index is constrained by the minimum micro-series length required by the embedding and multi-horizon settings, i.e.,

$$t_{\text{start}} = \max\{10, L + h_{\max}\}, \quad (11)$$

with look-back length $L = 5$ and $h_{\max} = 5$ in the present setup. The raw proxy profile $\lambda_1^{\text{raw}}(t)$ is additionally smoothed using a trailing-mean filter of window size $W_{\text{smooth}} = 4$, yielding $\tilde{\lambda}_1(t)$, which is used for metric computation. The primary learning target is the smoothed-profile reliability score S_{mom} (defined in the Profile-Based Reliability Metrics subsection), interpreted as a scalar indicator of early and strong contractive behavior and used to rank (α, β) configurations in terms of expected solver reliability.

3.5 Multi-Horizon Learning Protocol

For each grid point, learning features are constructed from the raw profile prefix $X_T = [\lambda_1^{\text{raw}}(1), \dots, \lambda_1^{\text{raw}}(T)]$ with horizons scanned as

$$T \in \{1, 1 + \Delta_T, 1 + 2\Delta_T, \dots\}, \quad (12)$$

up to the available profile length (with a fixed step Δ_T). Each horizon T defines an independent regression task mapping $X_T \mapsto S_{\text{mom}}$, enabling an "early-exit" assessment of predictive performance as a function of the amount of early information used.

3.6 Train/Test Splits and Evaluation

We evaluate generalization using two complementary train/test splitting strategies: (i) a random split over all grid points with a fixed test fraction of 40%, and (ii) a center-to-periphery split, where training uses the most central fraction of grid points in (α, β) space and testing uses peripheral points. For each split and each horizon T , model performance is reported on the held-out test set using MAE, RMSE, and R^2 .

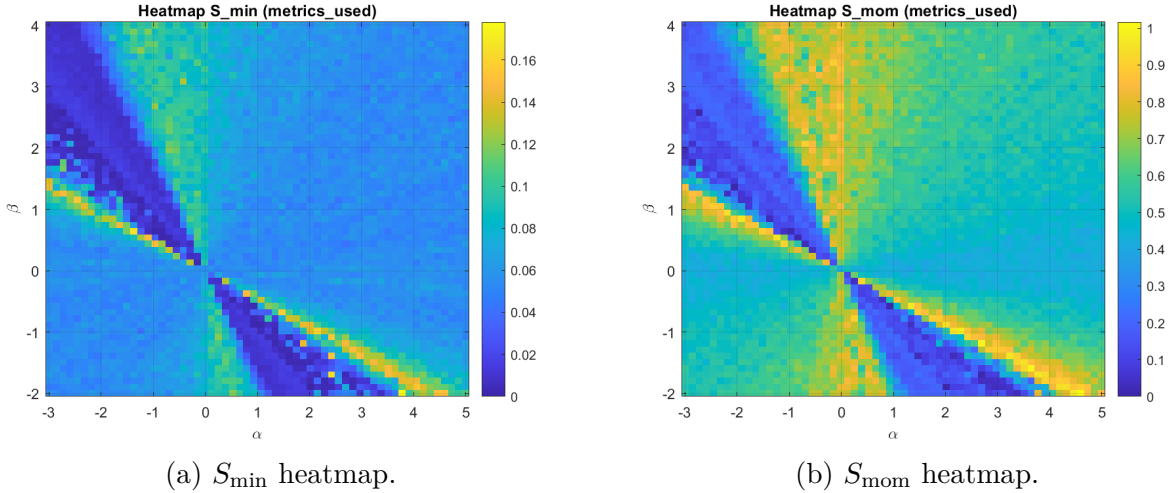


Figure 2: Ground-truth heatmaps of profile-based reliability metrics over the (α, β) grid: (a) S_{\min} and (b) S_{mom} .

4 Results

4.1 Ground-Truth Distributions of S_{\min} and S_{mom}

Figure 2 reports the ground-truth heatmaps of the two profile-based reliability metrics over the (α, β) grid. The maps exhibit a highly structured landscape with distinct parameter regions associated with stronger contractive behavior (higher scores) versus weaker or delayed contractivity (lower scores). In particular, S_{mom} provides a clear, interpretable ranking of parameter configurations, highlighting a stable "good" region that is consistently separated from less reliable regimes.

4.2 Representative kNN–LLE proxy profiles across the S_{mom} scale

To qualitatively illustrate how the kNN–LLE proxy profile varies across the parameter domain, we select six representative grid points spanning the full observed range of S_{mom} (ordered by increasing S_{mom}). Figure 3 shows raw and smoothed proxy profiles $\lambda_1(t_{\text{end}})$ for each selected point.

A clear qualitative trend is observed: low- S_{mom} cases tend to exhibit predominantly non-contractive behavior (profiles largely nonnegative or only weakly negative), often with delayed and shallow minima (large t_{\min}). In contrast, high- S_{mom} cases display an earlier and deeper negative excursion, yielding a pronounced minimum and a larger negative mass concentrated at small t_{end} . These visual patterns support the interpretability of S_{mom} as an "early-and-strong contractivity" indicator.

Importantly, the learning task addressed in this work is not to recompute S_{mom} from the full profile, but to predict S_{mom} from only an initial prefix of the raw curve (multi-horizon setting), i.e., before the minimum is necessarily observed.

4.3 Timing Statistics of Contractivity Signatures

To characterize when contractive behavior typically emerges, we analyze timing statistics derived from the smoothed proxy profile $\tilde{\lambda}_1(t)$. We define a "good" subset as the top 20% of grid points ranked by S_{mom} , yielding a threshold $S_{\text{mom}} \geq 0.6638$ (720 points out of 3600). For this good subset, the median location of the profile minimum is $t_{\min} = 21$ (corresponding to the profile index $T_{\min} \approx 12$ on the discrete t_{end} axis). This indicates that, in the good region, the characteristic

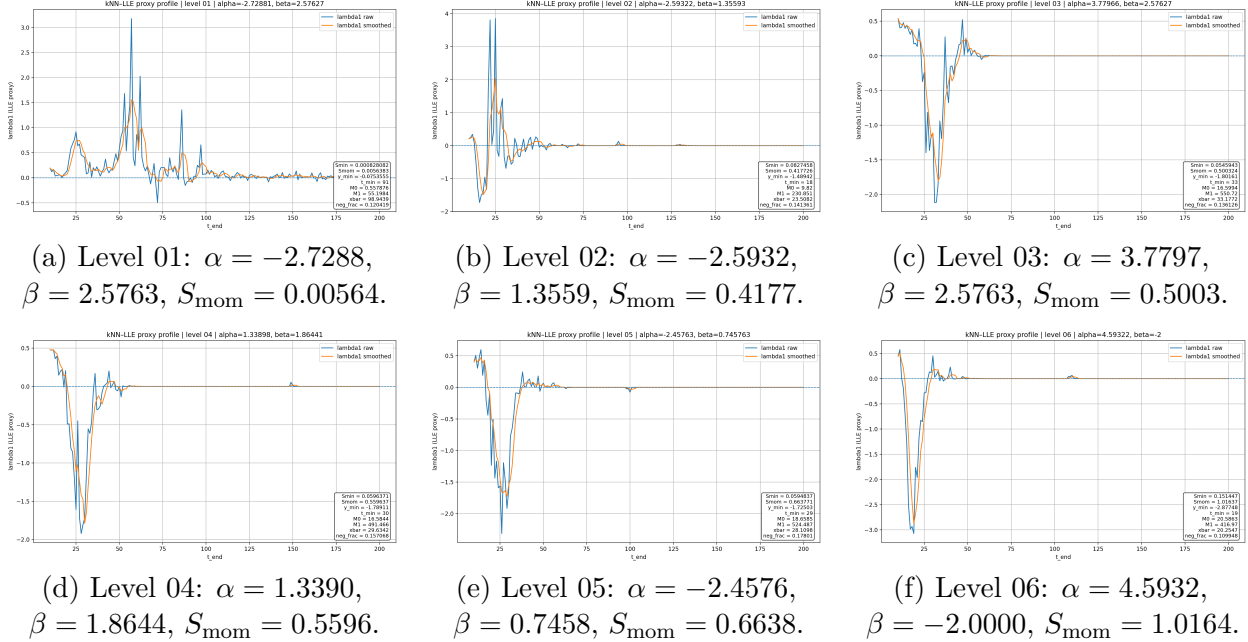


Figure 3: Representative kNN-LLE proxy profiles (raw vs. smoothed) spanning increasing S_{mom} levels (a)–(f). Higher S_{mom} typically corresponds to earlier and deeper contractive dips (more negative values) in the smoothed profile, whereas low S_{mom} cases tend to exhibit weak or delayed contractivity.

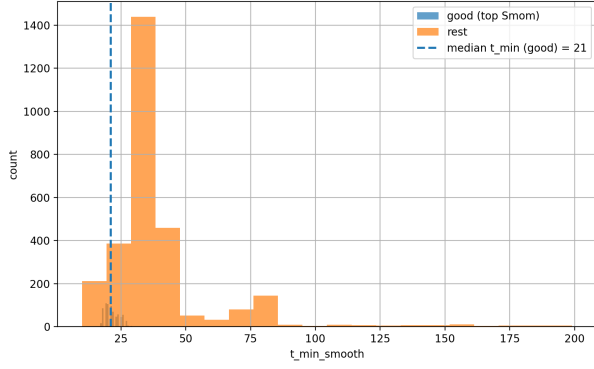
contractivity minimum occurs relatively early, supporting the multi-horizon viewpoint where reliable discrimination can be achieved using only the initial portion of the profile.

Figure 4 compares two timing distributions between the good subset and the remaining points: (i) the first time index at which $\tilde{\lambda}_1(t)$ becomes negative ($t_{\text{enter_neg}}$), and (ii) the minimum location t_{min} . The good subset tends to enter the negative (contractive) regime earlier and exhibits a more concentrated distribution of t_{min} , whereas the remaining region shows broader, often delayed timing patterns.

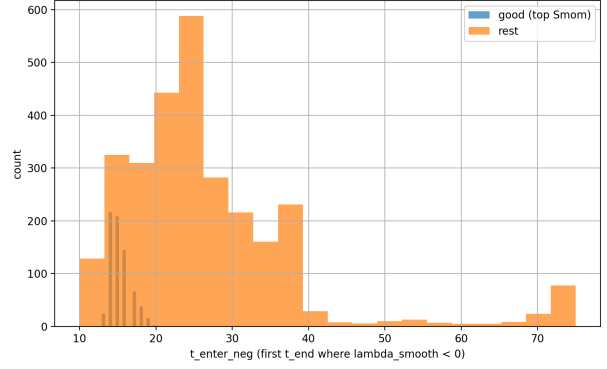
4.4 Multi-Horizon Regression Results (Center-to-Periphery Split)

We next evaluate the multi-horizon learning problem under the center-to-periphery split, where training samples are drawn from the most central region of the (α, β) grid and testing is performed on the periphery. This split probes out-of-distribution generalization across the parameter domain. All performance curves are reported as a function of the prefix length T (number of early raw proxy values $\lambda_1^{\text{raw}}(1:T)$ used as input), and are shown up to $T \leq 3T_{\text{min}}$, where $T_{\text{min}} = 12$ denotes the median minimum-location index of the good region (Figure 4).

Accuracy vs. horizon. Figure 5 summarizes MAE, RMSE, and R^2 as functions of T for all considered regressors. A consistent trend is observed: prediction quality improves rapidly with increasing horizon and then gradually saturates. Notably, strong predictive performance is achieved already around the characteristic minimum-location scale ($T \approx T_{\text{min}}$), supporting the feasibility of early reliability estimation before the full profile minimum is necessarily observed. Across horizons, nonlinear models (kNN and tree ensembles) substantially outperform linear baselines (Ridge/ElasticNet), especially for short prefixes, indicating that the mapping from early proxy

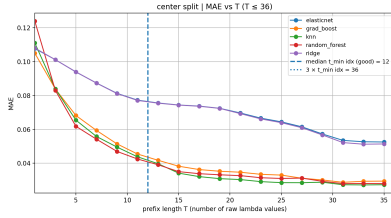


(a) Histogram of t_{\min} (smoothed profile).

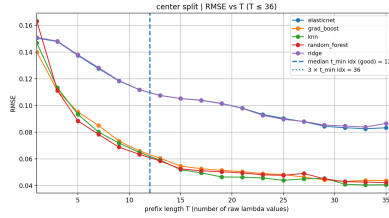


(b) Histogram of $t_{\text{enter_neg}}$ (first $\tilde{\lambda}_1(t) < 0$).

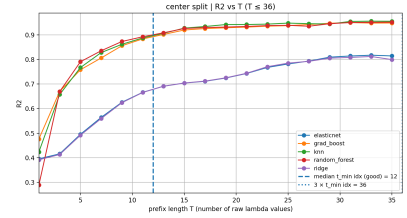
Figure 4: Timing statistics for the smoothed proxy profile $\tilde{\lambda}_1(t)$, comparing the good subset (top 20% by S_{mom}) against the rest: (a) distribution of the minimum location t_{\min} ; (b) distribution of the first negative entry time $t_{\text{enter_neg}}$.



(a) MAE vs. T .



(b) RMSE vs. T .



(c) R^2 vs. T .

Figure 5: Center split: prediction performance for S_{mom} as a function of prefix length T , reported up to $T \leq 3T_{\min} = 36$. The dashed line indicates $T_{\min} = 12$ (median minimum-location index of the good region), and the dotted line indicates $3T_{\min}$.

dynamics to S_{mom} is strongly nonlinear.

Best model per horizon. Table 1 lists the best-performing model (by R^2) for each scanned horizon $T \in \{1, 3, 5, \dots, 35\}$, together with the corresponding fit time and test-time inference costs. The selection varies with horizon: Gradient Boosting is preferred at the very smallest horizons, Random Forest dominates at intermediate horizons, and kNN becomes competitive at larger horizons. Overall, test-time costs remain small (microsecond to tens-of-microseconds per sample at this grid size), supporting the use of the learned diagnostic layer for early decision support.

Heatmap-level comparison (test-only predictions). To visualize spatial generalization, Figure 6 compares the theoretical S_{mom} landscape against test-only predicted heatmaps at representative horizons $T \in \{1, 3, 11\}$ using the best model selected at each horizon (Table 1). The training region is shown as white to emphasize out-of-sample behavior. As T increases, the predicted periphery increasingly recovers the main geometric structures of the true map, consistent with the monotone gains observed in Figure 5.

Table 1: Center split: best model by R^2 at each scanned horizon T . R^2 is rounded to three decimals; timing values are reported in seconds (scientific notation, two decimals).

T	best model	R^2	fit time (s)	test time (s)	test per-sample (s)
1	grad_boost	0.476	2.91e-01	3.06e-03	2.12e-06
3	grad_boost	0.670	6.30e-01	3.05e-03	2.12e-06
5	random_forest	0.791	3.12e-01	5.00e-02	3.47e-05
7	random_forest	0.836	3.46e-01	9.87e-02	6.85e-05
9	random_forest	0.873	3.67e-01	4.93e-02	3.42e-05
11	random_forest	0.893	4.48e-01	4.90e-02	3.40e-05
13	random_forest	0.909	4.48e-01	4.93e-02	3.43e-05
15	knn	0.928	5.41e-03	3.76e-02	2.61e-05
17	knn	0.934	8.12e-04	2.68e-02	1.86e-05
19	knn	0.942	1.04e-03	2.36e-02	1.64e-05
21	knn	0.942	1.18e-03	2.42e-02	1.68e-05
23	knn	0.944	1.08e-03	2.28e-02	1.59e-05
25	knn	0.948	1.10e-03	2.33e-02	1.62e-05
27	knn	0.946	1.37e-03	2.66e-02	1.85e-05
29	grad_boost	0.946	2.87e-01	3.28e-03	2.28e-06
31	knn	0.955	1.17e-03	2.35e-02	1.63e-05
33	knn	0.956	1.19e-03	2.41e-02	1.67e-05
35	knn	0.956	1.18e-03	2.39e-02	1.66e-05

4.5 Multi-Horizon Regression Results (Random Split)

Under the random split, training and test samples are drawn from the same global distribution over the parameter grid. Figure 7 reports MAE, RMSE, and R^2 as functions of horizon T , again truncated at $T \leq 3T_{\min} = 36$ for visual comparability with the center-split analysis. The overall behavior mirrors that of the center-to-periphery split: prediction quality improves sharply at small horizons and then gradually saturates. The absolute metrics are slightly better than in the center split, as expected in a less extrapolative setting, but the qualitative pattern remains the same.

Best model per horizon. Table 2 lists the best-by- R^2 model at each scanned horizon under the random split. The same main pattern appears as in the center split: Gradient Boosting is strongest at the very shortest horizons, while Random Forest and kNN dominate most larger horizons. Test-time inference remains negligible.

Heatmap-level comparison (test-only predictions). Figure 8 presents test-only predicted heatmaps for representative horizons $T \in \{1, 3, 11\}$ under the random split, using the corresponding best models from Table 2. Because the train/test partition is spatially interspersed, the training region appears as a punctured white mask rather than a contiguous block. Nevertheless, as T increases, the predicted values on the held-out points increasingly reproduce the true landscape of S_{mom} .

4.6 Computational Benefit of Early Prediction

The practical role of the predictive layer is not to compute the roots themselves, nor to optimize the initial guesses, but to screen parameter configurations (α, β) by predicting the final reliability score S_{mom} from an early prefix of the proxy profile. This distinction is important: the computational saving arises from avoiding the cost of generating the full diagnostic profile for every parameter pair. In the present setup, the full ground-truth diagnostic at a single grid point uses $K = 200$ solver iterations per trajectory. By contrast, a predictor operating at prefix length T requires only the

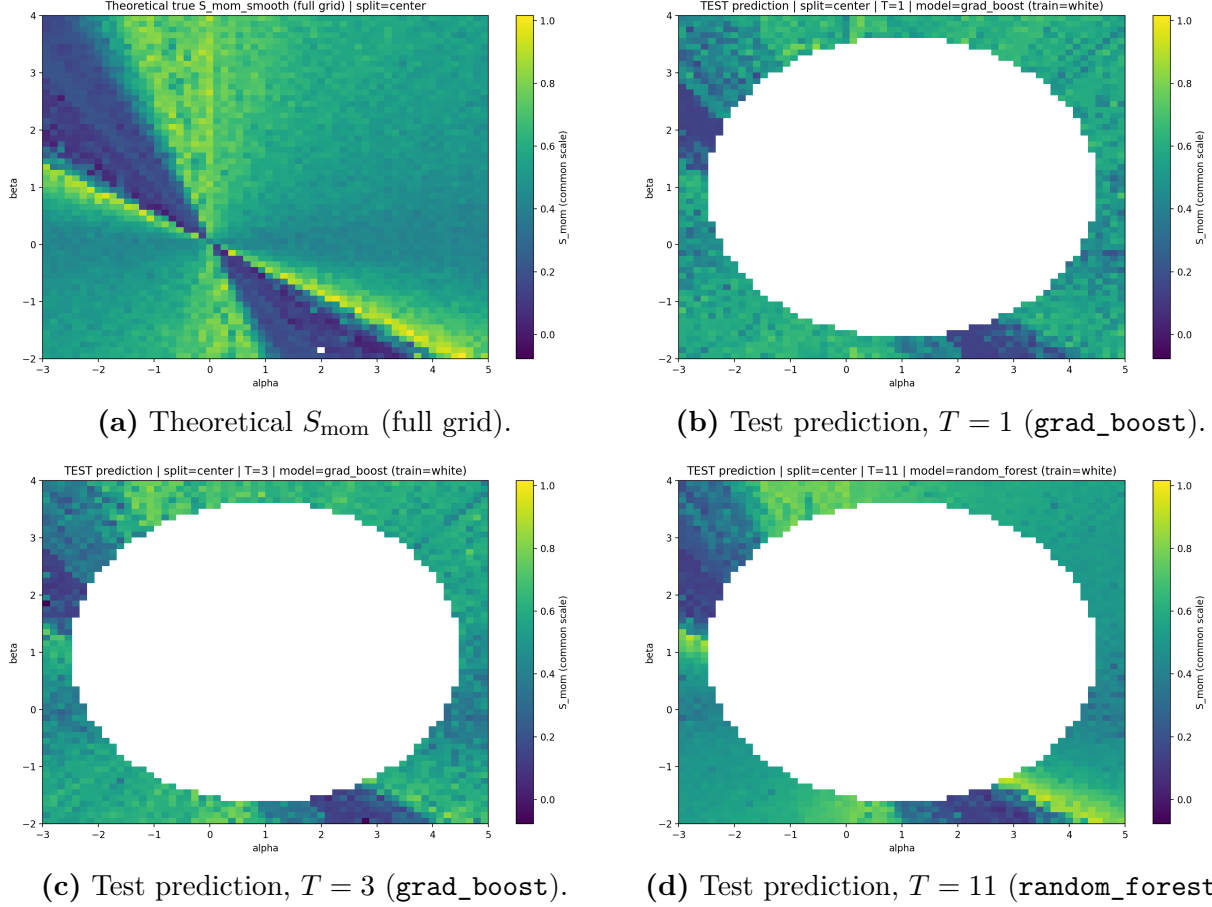


Figure 6: Center split: heatmap-level comparison between the theoretical S_{mom} landscape (a) and test-only predictions at increasing horizons (b)–(d). White region indicates training points (not plotted), while colored pixels correspond to test-region predictions on a common scale.

initial portion of the proxy profile. Because each proxy value $\lambda_1(t_{\text{end}})$ is itself built from a delay embedding of length $L = 5$ and forecast horizons up to $h_{\text{max}} = 5$, the horizon index T does not correspond one-to-one to the raw solver iteration count. A simple accounting gives an approximate requirement of

$$k_{\text{req}}(T) \approx T + L + h_{\text{max}} - 1 = T + 9, \quad (13)$$

solver iterations per trajectory in the current configuration. Therefore, the relative diagnostic cost at horizon T is approximately $(T + 9)/200$, and the corresponding speedup with respect to the full diagnostic is about $200/(T + 9)$.

Table 3 combines this cost estimate with the observed predictive quality at representative horizons. The results show that useful accuracy is achieved very early. In particular, at $T = 11$, which is close to the characteristic minimum-location scale identified from the good-region timing statistics, the predictive layer already achieves $R^2 \approx 0.89\text{--}0.91$ while using only about 20 solver iterations instead of the full 200. This corresponds to an approximately tenfold reduction in diagnostic cost per trajectory. Even the coarser horizon $T = 3$ requires only about 12 solver iterations, yielding an approximately $16.7\times$ reduction in solver budget while still recovering a useful fraction of the final reliability landscape.

This cost reduction is particularly relevant for screening unfavorable parameter configurations. The

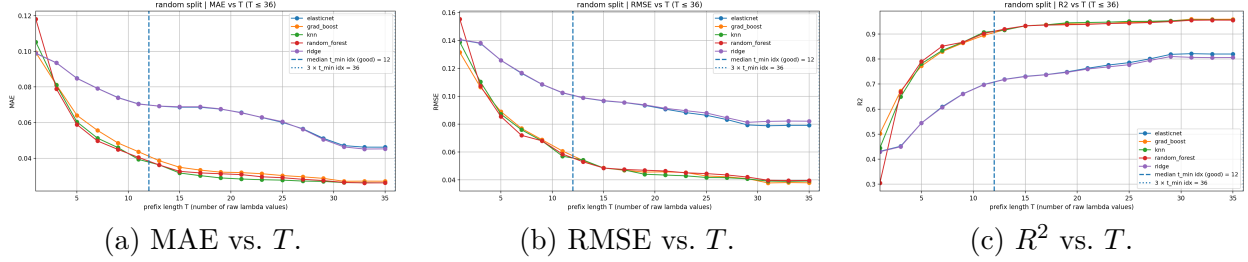


Figure 7: Random split: prediction performance for S_{mom} as a function of prefix length T , reported up to $T \leq 3T_{\text{min}} = 36$. The dashed line indicates $T_{\text{min}} = 12$, and the dotted line indicates $3T_{\text{min}}$.

Table 2: Random split: best model by R^2 at each scanned horizon T . R^2 is rounded to three decimals; timing values are reported in seconds (scientific notation, two decimals).

T	best model	R^2	fit (s)	test (s)	test/sample (s)
1	grad_boost	0.486	3.00e-01	3.41e-03	2.37e-06
3	grad_boost	0.673	4.57e-01	3.44e-03	2.39e-06
5	random_forest	0.791	3.00e-01	5.00e-02	3.47e-05
7	knn	0.852	2.50e-03	2.61e-03	1.81e-06
9	knn	0.879	2.54e-03	2.54e-03	1.76e-06
11	knn	0.905	2.53e-03	2.50e-03	1.74e-06
13	random_forest	0.919	4.36e-01	1.01e-01	7.01e-05
15	knn	0.931	2.44e-03	2.42e-03	1.68e-06
17	grad_boost	0.933	9.75e-01	3.28e-03	2.28e-06
19	knn	0.935	2.45e-03	2.39e-03	1.66e-06
21	knn	0.939	2.47e-03	2.44e-03	1.69e-06
23	knn	0.941	2.54e-03	2.62e-03	1.82e-06
25	knn	0.945	2.56e-03	2.44e-03	1.69e-06
27	knn	0.944	2.63e-03	2.56e-03	1.78e-06
29	knn	0.944	2.64e-03	2.45e-03	1.70e-06
31	grad_boost	0.956	1.12e00	3.20e-03	2.22e-06
33	grad_boost	0.957	1.13e00	3.25e-03	2.25e-06
35	grad_boost	0.958	1.17e00	3.22e-03	2.24e-06

timing histograms in Figure 4 show that the characteristic profile events used by the full diagnostic, such as the minimum of $\tilde{\lambda}_1(t)$ and the first entry into the negative regime, are not uniformly early across the parameter grid. In less favorable regions, these events can occur substantially later than in the good subset, so waiting for the complete profile delays the rejection of poor parameter choices. By contrast, the learned predictor can issue an informative estimate of the eventual S_{mom} score from a much shorter prefix. In this sense, the proposed AI layer does not accelerate the underlying root-finding iterations themselves; rather, it accelerates the reliability assessment and parameter screening process built on top of the solver.

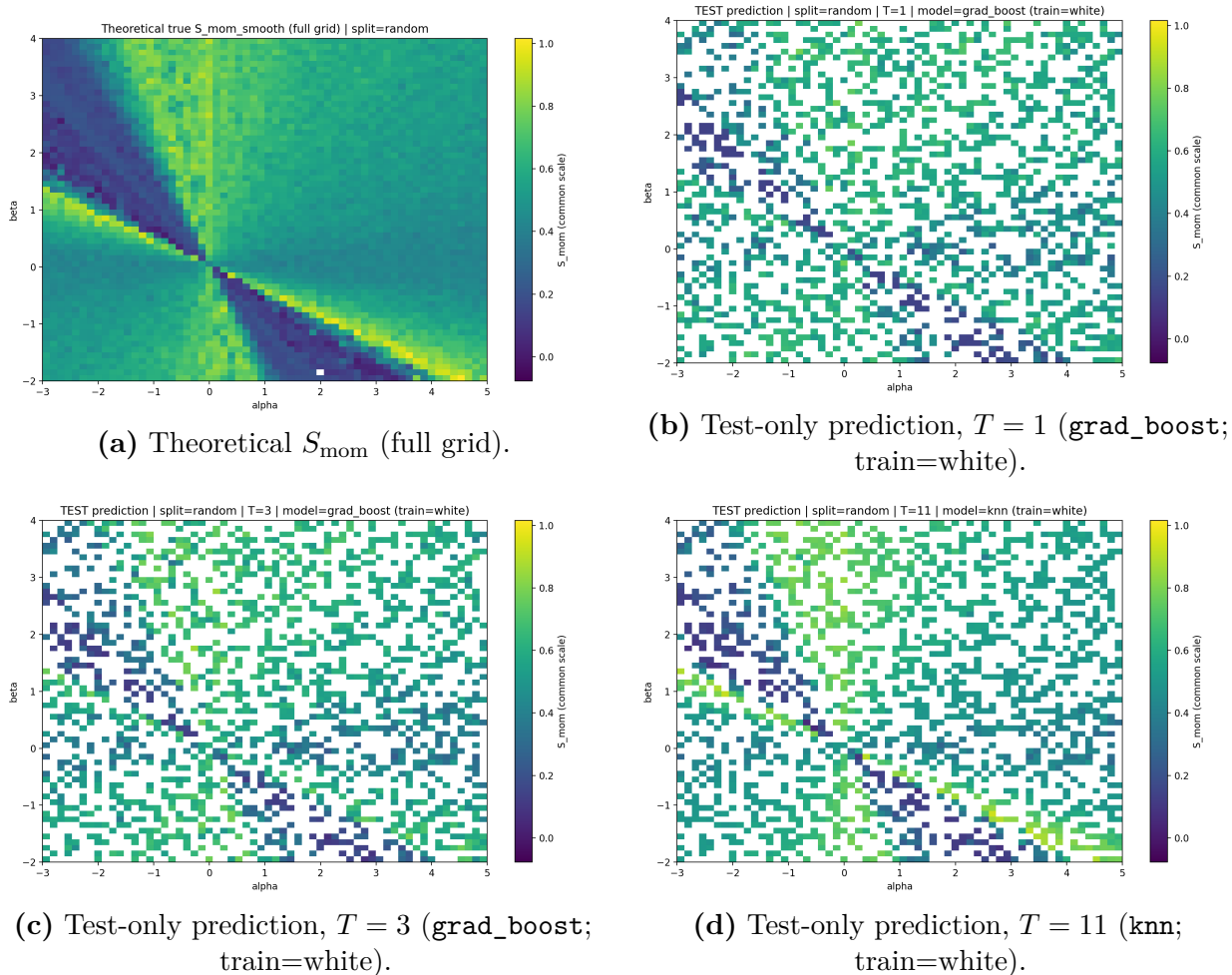


Figure 8: Random split: heatmap-level comparison between the theoretical S_{mom} landscape (a) and test-only predictions at increasing horizons (b)–(d). White cells indicate training points (not plotted), while colored cells correspond to test-region predictions on a common scale.

Table 3: Approximate diagnostic cost versus predictive quality at representative horizons. The solver-iteration requirement is estimated as $k_{\text{req}}(T) \approx T + 9$ for the present proxy construction ($L = 5$, $h_{\text{max}} = 5$), and the full diagnostic uses $K = 200$ iterations per trajectory.

T	approx. solver iterations	speedup vs. full $K = 200$	center split R^2	random split R^2
1	10	20.0×	0.476	0.486
3	12	16.7×	0.670	0.673
11	20	10.0×	0.893	0.905
35	44	4.5×	0.956	0.958

5 Discussion

The results demonstrate that short prefixes of kNN–LLE proxy profiles contain substantial information about the final reliability score S_{mom} , making early prediction feasible across a structured two-parameter solver landscape. Beyond the raw regression metrics, several points deserve further interpretation.

Why early prediction works. The proxy profile is designed to summarize local contractivity and expansivity trends in the iteration dynamics. The empirical curves in Figures 5 and 7 exhibit a common pattern: a steep accuracy gain at small prefix lengths T , followed by a gradual saturation. This behavior is consistent with the role of S_{mom} as an early-and-strong contractivity indicator: once the initial portion of the proxy dynamics reveals the onset (or absence) of contractive tendencies, additional late-profile information yields diminishing improvements.

Interpretability of the predictive layer. An important feature of the proposed framework is that the machine learning models do not operate directly on raw solver iterates or full iteration trajectories. Instead, they use early prefixes of the kNN–LLE proxy profile, which encode interpretable local stability signatures of the underlying dynamics. In this sense, the predictive layer remains connected to the dynamical interpretation of solver behavior: the learned mapping is not from arbitrary high-dimensional traces to a score, but from contractive/expansive profile patterns to the final reliability indicator S_{mom} . This makes the approach more transparent than a purely black-box surrogate built directly on raw iteration data.

Prediction before the characteristic minimum scale ($T < T_{\text{min}}$). A key practical regime is prediction before the typical minimum-location index of the good region, $T_{\text{min}} = 12$. This corresponds to forecasting reliability before the visually apparent minimum of the smoothed proxy profile is necessarily observed. In both splits, strong accuracy is already achieved around $T \approx T_{\text{min}}$, indicating that reliable discrimination is possible from early signatures alone. This is particularly important for early decision support, where the goal is to avoid spending the full computational budget required to reach the minimum if an unfavorable configuration can be detected earlier.

The extreme early-exit case $T = 1$. The $T = 1$ setting is especially notable: the model receives only the first raw proxy value $\lambda_1^{\text{raw}}(1)$. Despite being a single scalar, this quantity is not a trivial instantaneous measurement. In the underlying kNN–LLE construction, each $\lambda_1(t_{\text{end}})$ value is produced from a delay-embedding of length L and a multi-horizon forecast over $h \in \{1, \dots, 5\}$, so the earliest proxy estimate already aggregates information from a short history and multiple forward steps. In that sense, $T = 1$ still represents a compressed summary of early solver dynamics rather than a single iteration of the base root-finding scheme. Nevertheless, the errors at $T = 1$ remain larger than for $T \geq 3$, and the heatmap comparisons confirm that very short horizons capture only coarse structures. This suggests that while a one-step diagnostic is feasible, a modest prefix length ($T \approx 3\text{--}5$) provides a substantially more reliable and stable prediction regime.

Random vs. center-to-periphery generalization. The two splitting strategies yield broadly comparable quantitative accuracy, but they probe different notions of generalization. The random split evaluates within-distribution performance, and the associated test-only heatmaps appear spatially punctured because the training region is interspersed throughout the domain. In contrast, the center-to-periphery split enforces a structured extrapolation test: the models are trained on

central parameter regimes and evaluated on boundary regimes, which is more representative of out-of-distribution deployment scenarios (e.g., screening untested parameter regions or transferring to nearby regimes). The fact that the center split still achieves high R^2 at moderate horizons supports the robustness of the learned mapping across the parameter domain, although the visual recovery of fine geometric details is naturally slower than in the i.i.d. case.

Model behavior and inductive biases. Across both splits, nonlinear regressors (kNN, Gradient Boosting, Random Forest) consistently dominate the linear baselines (Ridge and Elastic Net), particularly at short horizons. This indicates that the mapping from early proxy dynamics to S_{mom} is strongly nonlinear and regime-dependent. Ridge and Elastic Net provide stable baselines under correlated features, but their limited expressivity is reflected by systematically lower R^2 and their absence from best-by- T selections. Among nonlinear models, the differences are comparatively small on the metric curves, suggesting that several model families can approximate the target mapping well once sufficient prefix information is available. The best-by- T tables show that model preference can shift with horizon: boosting methods can be advantageous at extremely small horizons, while kNN or Random Forest becomes competitive as T increases. Importantly, regardless of the chosen model, inference costs remain negligible relative to the profile-generation pipeline, reinforcing the viability of using the predictor as a lightweight reliability layer.

Heatmap-level interpretation. The heatmap comparisons provide an interpretable spatial validation beyond scalar metrics. For small horizons, predicted maps reproduce only large-scale features (e.g., broad high-score ridges and low-score wedges), while increasing T progressively restores the geometry of the theoretical landscape. This qualitative improvement is consistent with the monotone gains in MAE/RMSE and R^2 . Under center-to-periphery splitting, the predicted boundary region becomes visually close to the theoretical map at moderate horizons, which is the desired behavior for screening unseen parameter regions.

Generality beyond a specific equation and open questions. A central motivation of the proposed diagnostic layer is that it relies on observable dynamics (proxy contractivity profiles) rather than closed-form properties of a particular nonlinear equation. Consequently, the approach is expected to be less equation-specific than direct surrogate modeling of solver outputs. In principle, a model trained on one problem class may transfer to another, provided the early proxy profiles encode comparable stability signatures; however, this transferability requires dedicated validation. Future work should therefore test cross-problem generalization (training on one equation/model family and evaluating on another) and quantify how changes in profiling hyperparameters (L , horizon set, smoothing width) affect stability of the learned mapping and the best-by- T selection.

Possible applications in systems biology and related steady-state studies. A particularly promising application perspective of the proposed framework arises in parameterized steady-state problems from systems biology and related areas. In biochemical reaction networks, metabolic ODE models, and signaling systems, biologically relevant steady states are often computed repeatedly across many parameter configurations for parameter estimation, sensitivity analysis, bifurcation studies, or regime screening [24, 25, 26, 27]. In such settings, repeated nonlinear solves can become a major computational bottleneck, and convergence may depend strongly on the parameter regime and on the numerical behavior of the solver.

From this viewpoint, the present diagnostic layer could serve as an early screening tool for repeated steady-state computations. Rather than replacing the underlying nonlinear solver, it could help

identify parameter regions that are numerically favorable, likely to yield stable steady states, or conversely prone to instability or wasted computational effort. This perspective is also consistent with recent literature on stability-constrained parameter exploration and parameter-space partitioning in biological models [28, 29, 30]. At the same time, the current paper does not yet demonstrate such an application directly; this should therefore be regarded as a realistic and literature-supported direction for future work rather than as a validated biological case study.

Summary of main observations.

- Predictive accuracy improves rapidly with horizon T and saturates thereafter; strong performance emerges near the characteristic scale $T_{\min} = 12$, enabling early reliability prediction before the typical minimum is observed.
- The $T = 1$ regime is feasible but relatively noisy; modest horizons ($T \approx 3\text{--}5$) provide a more reliable early-exit operating point.
- Nonlinear models (kNN and tree ensembles) substantially outperform linear baselines (Ridge/Elastic Net), indicating a strongly nonlinear mapping from early proxy dynamics to S_{mom} .
- Random and center-to-periphery splits yield broadly comparable accuracy, while the center split provides a more stringent test of out-of-distribution generalization across the parameter domain.
- Heatmap-level comparisons confirm that increasing T yields progressively more faithful recovery of the true spatial reliability landscape, supporting the interpretability and practical utility of the proposed diagnostic layer.

6 Conclusion

We presented an interpretable AI-assisted reliability diagnostic for a two-parameter parallel root-finding scheme, combining kNN–LLE proxy profiling with multi-horizon prediction of the profile-derived score S_{mom} . The study shows that short early prefixes of the raw proxy profile already contain sufficient information to predict the final reliability score with high accuracy across the (α, β) parameter domain, including under the more demanding center-to-periphery split.

The main practical consequence is that reliability screening can be performed well before the full proxy profile is available. In the present experiments, prediction at $T = 11$ achieves $R^2 \approx 0.89\text{--}0.91$ while requiring only about one tenth of the full solver budget needed to compute the complete diagnostic profile. This makes the proposed layer suitable for early rejection of unfavorable parameter configurations and for integrating lightweight decision support into solver workflows. Future work will focus on cross-problem transfer, robustness with respect to profiling hyperparameters, and adaptive policies that couple the learned diagnostic directly to runtime solver control.

A Auxiliary Solver Validation of the Base Scheme

This appendix collects solver-level validation results that support the numerical quality of the underlying parallel scheme but are not part of the main predictive contribution of the paper. All experiments in this appendix are performed at the fixed representative parameter pair $(\alpha, \beta) = (-0.1, 4.0)$, chosen from the stable region of the (α, β) landscape.

To examine the robustness of the iterative scheme, three initialization strategies are used:

Near-root:

$$z_k^{(0)} = \alpha_k + 10^{-2}\varepsilon_k, \quad \varepsilon_k \in [-1, 1], \quad k = 1, \dots, 7.$$

Moderate:

$$z_k^{(0)} = r e^{\frac{2\pi i(k-1)}{7}}, \quad r = 5, \quad k = 1, \dots, 7.$$

Random:

$$z_k^{(0)} \sim \mathcal{U}([-10, 10] + i[-10, 10]), \quad k = 1, \dots, 7.$$

A.1 Sensitivity to Initial Guesses

The convergence behavior of simultaneous root-finding methods depends on the quality of the initial approximations. To illustrate the robustness of the base solver under different starts, we consider three initialization scenarios: near-root initialization, moderately distant initialization, and random initialization. For each case, we monitor the maximum per-root error at iteration k ,

$$E^{(k)} = \max_{1 \leq i \leq n} |z_i^{(k)} - \xi_i|. \quad (14)$$

The corresponding convergence histories are shown in Figure 9, while Table 4 summarizes the early-iteration error decay.

Table 4: Early iteration error behavior of the proposed scheme under different initialization scenarios.

Iteration k	Near-root init.	Moderate init.	Random init.	Order (approx.)
1	1.26×10^{-2}	3.35×10^{-1}	8.44×10^{-1}	—
2	2.86×10^{-7}	5.71×10^{-5}	3.47×10^{-4}	3.92
3	4.66×10^{-21}	7.44×10^{-9}	9.78×10^{-10}	4.15
4	2.16×10^{-59}	2.43×10^{-17}	4.72×10^{-27}	4.97
5	6.38×10^{-75}	8.04×10^{-49}	7.01×10^{-25}	5.67
6	9.17×10^{-191}	0.21×10^{-160}	3.47×10^{-90}	5.97

The appendix experiment confirms that closer initial guesses accelerate the entrance into the asymptotic high-order regime, while even moderate or random starts still produce very rapid error decay within a few iterations. This observation is useful for documenting the numerical behavior of the underlying solver, but it should be interpreted separately from the main contribution of the present paper, which concerns prediction of S_{mom} across the parameter space.

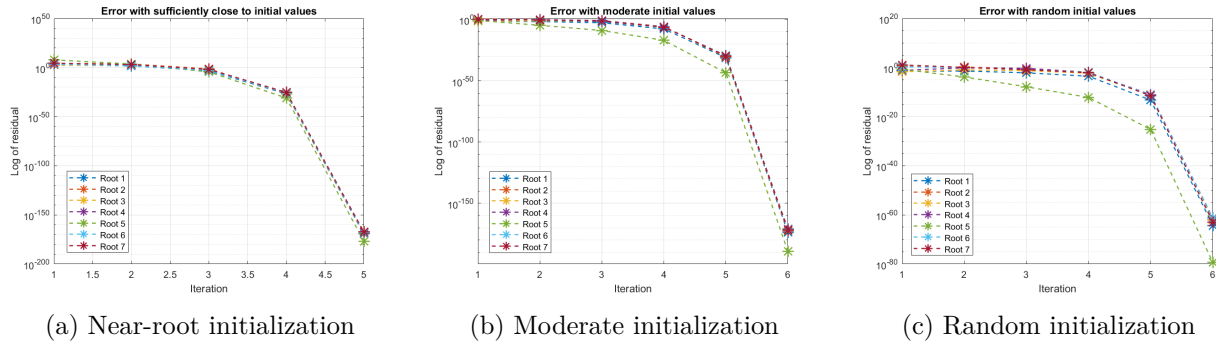


Figure 9: Early-iteration convergence of the proposed parallel scheme under different initialization scenarios, showing $\log_{10}(E^{(k)})$ versus iteration index.

A.2 Comparison with Existing Parallel Schemes

For completeness, we also report a compact comparison between the proposed scheme and two existing parallel methods from the literature. Table 5 summarizes the number of iterations to convergence, CPU time, memory usage, and maximum error, while Table 6 reports theoretical and observed convergence orders.

Table 5: Computational performance of the proposed solver.

Method	Iterations	CPU time (s)	Memory (MB)	Maximum error
Proposed Scheme [21]	5	0.012	123.65	2.05×10^{-189}
Existing Scheme [31]	11	0.018	256.76	5.14×10^{-45}
Existing Scheme [32]	10	0.015	254.89	0.77×10^{-37}

Table 6: Estimated convergence order of the methods.

Method	Order (theoretical)	Order (observed)
Proposed Scheme [21]	6	5.97
Existing Scheme [31]	6	4.56
Existing Scheme [32]	6	3.19

These appendix results indicate that the proposed base scheme converges in fewer iterations and attains markedly smaller final errors than the two comparison methods, while preserving an observed order close to the theoretical sixth order. Again, this comparison is intended only as auxiliary solver validation. The main manuscript focuses instead on the AI-assisted diagnostic layer that predicts profile-based reliability over the (α, β) domain.

Funding

The work reported in Sections 3 and 4 was supported by the Russian Science Foundation (grant no. 22-11-00055-P, <https://rscf.ru/en/project/22-11-00055/>, accessed on 10 June 2025) (Andrei Velichko). The material reported in Sections 1 and 5 was supported by the European Regional Development and Cohesion Funds (ERDF) 2021–2027 under Project AI4AM - EFRE1052 (Bruno Carpentieri). Bruno Carpentieri is also a member of the *Gruppo Nazionale per il Calcolo Scientifico* (GNCS) of the *Istituto Nazionale di Alta Matematica* (INdAM).

Author contributions

Conceptualization: Bruno Carpentieri, Andrei Velichko, Mudassir Shams; Methodology: Bruno Carpentieri, Andrei Velichko, Mudassir Shams; Software: Andrei Velichko, Mudassir Shams; Validation: Bruno Carpentieri, Andrei Velichko, Mudassir Shams; Formal analysis: Bruno Carpentieri; Investigation: Bruno Carpentieri, Andrei Velichko, Mudassir Shams; Data curation: Andrei Velichko, Mudassir Shams; Writing—original draft: Bruno Carpentieri, Andrei Velichko, Mudassir Shams; Writing—review & editing: Bruno Carpentieri, Andrei Velichko, Paola Lecca; Visualization: Andrei Velichko, Mudassir Shams; Supervision: Bruno Carpentieri, Andrei Velichko; Project administration: Bruno Carpentieri. All authors have read and agreed to the submitted version of the manuscript.

Disclosure of interest

The authors report no conflict of interest.

Data availability statement

All data products generated in this study (including grid-level metrics, raw and smoothed proxy profiles, train/test split manifests, model predictions, and aggregated summaries) are provided in the accompanying project directory. The implementation scripts and detailed reproduction instructions will be made publicly available in an online repository upon publication.

References

- [1] James M. Ortega and Werner C. Rheinboldt. *Iterative Solution of Nonlinear Equations in Several Variables*, volume 30 of *Classics in Applied Mathematics*. SIAM, Philadelphia, 2000. doi:[10.1137/1.9780898719468](https://doi.org/10.1137/1.9780898719468).
- [2] Tim C. Kelley. *Solving Nonlinear Equations with Newton's Method*. Society for Industrial and Applied Mathematics, Philadelphia, PA, 2003. doi:[10.1137/1.9780898718898](https://doi.org/10.1137/1.9780898718898).
- [3] John E. Dennis and Robert B. Schnabel. *Numerical Methods for Unconstrained Optimization and Nonlinear Equations*. Society for Industrial and Applied Mathematics, Philadelphia, PA, 1996. doi:[10.1137/1.9781611971200](https://doi.org/10.1137/1.9781611971200).
- [4] Miodrag S. Petković, Beny Neta, Ljiljana D. Petković, and Jovana Džunić. Multipoint methods for solving nonlinear equations: A survey. *Applied Mathematics and Computation*, 226:635–660, 2014. ISSN 0096-3003. doi:[10.1016/j.amc.2013.10.072](https://doi.org/10.1016/j.amc.2013.10.072).
- [5] Kaushal Kumar and Ekaterina Kostina. Optimal parameter estimation techniques for complex nonlinear systems. *Differential Equations and Dynamical Systems*, 2024. ISSN 0974-6870. doi:[10.1007/s12591-024-00688-9](https://doi.org/10.1007/s12591-024-00688-9). URL <https://doi.org/10.1007/s12591-024-00688-9>.
- [6] Fang-Rong Yan, Ping Zhang, Jun-Lin Liu, Yu-Xi Tao, Xiao Lin, Tao Lu, and Jin-Guan Lin. Parameter estimation of population pharmacokinetic models with stochastic differential equations: Implementation of an estimation algorithm. *Journal of Probability and Statistics*, 2014 (1):836518, 2014. doi:[10.1155/2014/836518](https://doi.org/10.1155/2014/836518). URL <https://doi.org/10.1155/2014/836518>.
- [7] James Keener and James Sneyd. *Mathematical Physiology I: Cellular Physiology*, volume 8 of *Interdisciplinary Applied Mathematics*. Springer, New York, 2 edition, 2009. ISBN 978-0-387-75847-3. doi:[10.1007/978-0-387-75847-3](https://doi.org/10.1007/978-0-387-75847-3).
- [8] Alfio Quarteroni, Riccardo Sacco, and Fausto Saleri. *Numerical Mathematics*, volume 37 of *Texts in Applied Mathematics*. Springer, Berlin, Heidelberg, 2 edition, 2007. ISBN 978-3-540-34658-6. doi:[10.1007/b98885](https://doi.org/10.1007/b98885).
- [9] Richard Creswell, Katherine M. Shepherd, Ben Lambert, Gary R. Mirams, Chon Lok Lei, Simon Tavener, Martin Robinson, and David J. Gavaghan. Understanding the impact of numerical solvers on inference for differential equation models. *Journal of The Royal Society Interface*, 21(212):20230369, 2024. ISSN 1742-5689. doi:[10.1098/rsif.2023.0369](https://doi.org/10.1098/rsif.2023.0369). URL <https://doi.org/10.1098/rsif.2023.0369>.

- [10] George E. Karniadakis, Ioannis G. Kevrekidis, Lu Lu, Paris Perdikaris, Sifan Wang, and Liu Yang. Physics-informed machine learning. *Nature Reviews Physics*, 3(6):422–440, 2021. ISSN 2522-5820. doi:[10.1038/s42254-021-00314-5](https://doi.org/10.1038/s42254-021-00314-5).
- [11] Mudassir Shams and Bruno Carpentieri. Efficient inverse fractional neural network-based simultaneous schemes for nonlinear engineering applications. *Fractal and Fractional*, 7(12), 2023. doi:[10.3390/fractalfract7120849](https://doi.org/10.3390/fractalfract7120849).
- [12] Mudassir Shams and Bruno Carpentieri. Q-analogues of parallel numerical scheme based on neural networks and their engineering applications. *Applied Sciences*, 14(4), 2024. ISSN 2076-3417. doi:[10.3390/app14041540](https://doi.org/10.3390/app14041540). URL <https://www.mdpi.com/2076-3417/14/4/1540>.
- [13] Diogo Freitas, Luiz Guerreiro Lopes, and Fernando Morgado-Dias. A neural network-based approach for approximating arbitrary roots of polynomials. *Mathematics*, 9(4), 2021. ISSN 2227-7390. doi:[10.3390/math9040317](https://doi.org/10.3390/math9040317). URL <https://www.mdpi.com/2227-7390/9/4/317>.
- [14] Qiuyue Zuo, Haibing Fan, Lin Xiao, and Zhizhong Liu. Two novel cold-start multistage neural solvers for constrained nonlinear equations with extended time horizons. *Neural Networks*, 192: 107917, 2025. ISSN 0893-6080. doi:[10.1016/j.neunet.2025.107917](https://doi.org/10.1016/j.neunet.2025.107917).
- [15] Maziar Raissi, Paris Perdikaris, and George E. Karniadakis. Physics-informed neural networks: A deep learning framework for solving forward and inverse problems involving nonlinear partial differential equations. *Journal of Computational Physics*, 378:686–707, 2019. ISSN 0021-9991. doi:[10.1016/j.jcp.2018.10.045](https://doi.org/10.1016/j.jcp.2018.10.045).
- [16] Lu Lu, Pengzhan Jin, Guofei Pang, Zhongqiang Zhang, and George E. Karniadakis. Learning nonlinear operators via DeepONet based on the universal approximation theorem of operators. *Nature Machine Intelligence*, 3(3):218–229, 2021. ISSN 2522-5839. doi:[10.1038/s42256-021-00302-5](https://doi.org/10.1038/s42256-021-00302-5).
- [17] Frank Hutter, Lars Kotthoff, and Joaquin Vanschoren, editors. *Automated Machine Learning: Methods, Systems, Challenges*. The Springer Series on Challenges in Machine Learning. Springer, Cham, 2019. ISBN 978-3-030-05317-8. doi:[10.1007/978-3-030-05318-5](https://doi.org/10.1007/978-3-030-05318-5).
- [18] Alan Wolf, Jack B. Swift, Harry L. Swinney, and John A. Vastano. Determining Lyapunov exponents from a time series. *Physica D: Nonlinear Phenomena*, 16(3):285–317, 1985. ISSN 0167-2789. doi:[10.1016/0167-2789\(85\)90011-9](https://doi.org/10.1016/0167-2789(85)90011-9).
- [19] Andrei Velichko, Maksim Belyaev, and Petr Boriskov. A novel approach for estimating largest Lyapunov exponents in one-dimensional chaotic time series using Machine Learning. *Chaos: An Interdisciplinary Journal of Nonlinear Science*, 35(10):101101, 2025. ISSN 1054-1500. doi:[10.1063/5.0289352](https://doi.org/10.1063/5.0289352).
- [20] Yazhini Muruganatham, Andrei Velichko, and Samidurai Rajendran. Local Lyapunov analysis via micro-ensembles: finite-time Lyapunov exponent estimation and KNN-based predictive comparison in complex-valued BAM neural networks, 2025. URL <https://arxiv.org/abs/2512.16179>.
- [21] Mudassir Shams, Andrei Velichko, and Bruno Carpentieri. Finite-time contractivity profiling of a two-parameter parallel root-finding scheme via a kNN–LLE proxy. *Mathematics*, 14(5): 879, 2026. ISSN 2227-7390. doi:[10.3390/math14050879](https://doi.org/10.3390/math14050879).

- [22] Mudassir Shams, Andrei Velichko, and Bruno Carpentieri. Direct finite-time contraction (step-log) profiling–driven optimization of parallel schemes for nonlinear problems on multicore architectures, 2026. URL <https://arxiv.org/abs/2601.13637>.
- [23] Nicholas McGreivy and Aman Hakim. Weak baselines and reporting biases lead to overoptimism in machine learning for fluid-related partial differential equations. *Nature Machine Intelligence*, 6:1256–1269, 2024. doi:[10.1038/s42256-024-00897-5](https://doi.org/10.1038/s42256-024-00897-5).
- [24] Glenn Terje Lines, Łukasz Paszkowski, Leonard Schmiester, Daniel Weindl, Paul Stapor, and Jan Hasenauer. Efficient computation of steady states in large-scale ODE models of biochemical reaction networks. *IFAC-PapersOnLine*, 52(26):32–37, 2019. ISSN 2405-8963. doi:[10.1016/j.ifacol.2019.12.232](https://doi.org/10.1016/j.ifacol.2019.12.232). 8th Conference on Foundations of Systems Biology in Engineering (FOSBE 2019).
- [25] Polina Lakrisenko, Paul Stapor, Stephan Grein, Łukasz Paszkowski, Dilan Pathirana, Fabian Fröhlich, Glenn Terje Lines, Daniel Weindl, and Jan Hasenauer. Efficient computation of adjoint sensitivities at steady state in ODE models of biochemical reaction networks. *PLOS Computational Biology*, 19(3):e1010948, 2023. doi:[10.1371/journal.pcbi.1010948](https://doi.org/10.1371/journal.pcbi.1010948).
- [26] Marcus Rosenblatt, Jens Timmer, and Daniel Kaschek. Customized steady-state constraints for parameter estimation in non-linear ordinary differential equation models. *Frontiers in Cell and Developmental Biology*, 4:41, 2016. ISSN 2296-634X. doi:[10.3389/fcell.2016.00041](https://doi.org/10.3389/fcell.2016.00041).
- [27] Anna Fiedler, Sebastian Raeth, Fabian J. Theis, Angelika Hausser, and Jan Hasenauer. Tailored parameter optimization methods for ordinary differential equation models with steady-state constraints. *BMC Systems Biology*, 10(1):80, 2016. ISSN 1752-0509. doi:[10.1186/s12918-016-0319-7](https://doi.org/10.1186/s12918-016-0319-7).
- [28] Yoshiaki Kariya, Masashi Honma, Keita Tokuda, Akihiko Konagaya, and Hiroshi Suzuki. Utility of constraints reflecting system stability on analyses for biological models. *PLOS Computational Biology*, 18(9):e1010441, 2022. doi:[10.1371/journal.pcbi.1010441](https://doi.org/10.1371/journal.pcbi.1010441).
- [29] Bryan S. Hernandez, Patrick Vincent N. Lubenia, Matthew D. Johnston, and Jae Kyoung Kim. A framework for deriving analytic steady states of biochemical reaction networks. *PLOS Computational Biology*, 19(4):e1011039, 2023. doi:[10.1371/journal.pcbi.1011039](https://doi.org/10.1371/journal.pcbi.1011039).
- [30] Russell Bradford, James H. Davenport, Matthew England, Hassan Errami, Vladimir Gerdt, Dima Grigoriev, Charles Hoyt, Marek Košta, Ovidiu Radulescu, Thomas Sturm, and Andreas Weber. Identifying the parametric occurrence of multiple steady states for some biological networks. *Journal of Symbolic Computation*, 98:84–119, 2020. ISSN 0747-7171. doi:[10.1016/j.jsc.2019.07.008](https://doi.org/10.1016/j.jsc.2019.07.008). Special Issue on Symbolic and Algebraic Computation: ISSAC 2017.
- [31] Rui N. Machado and Luís G. Lopes. A family of ehrlich-type accelerated methods with king’s correction for the simultaneous approximation of polynomial complex zeros. *Global Journal of Pure and Applied Mathematics*, 15(6):789–802, 2019. URL <https://digituma.uma.pt/entities/publication/67fbb94b-6ba4-4b0b-8224-6266a6efd356>.
- [32] Miodrag S. Petković, Ljiljana D. Petković, and Jovana Džunić. On an efficient method for the simultaneous approximation of polynomial multiple roots. *Applied Analysis and Discrete Mathematics*, 8(1):73–94, 2014. URL <https://www.jstor.org/stable/43666184>.

- [33] Joseph Cummings, Kyle J.-M. Dahlin, Elizabeth Gross, and Jonathan D. Hauenstein. Routing functions for parameter space decomposition to describe stability landscapes of ecological models. *Bulletin of Mathematical Biology*, 87(12):177, 2025. ISSN 1522-9602. doi:[10.1007/s11538-025-01554-7](https://doi.org/10.1007/s11538-025-01554-7).